Available online at www.sciencedirect.com
ScienceDirect
C. R. Mecanique 336 (2008) 149–162
COMPTES RENDUS MECANIQUE
http://france.elsevier.com/direct/CRAS2B/

Duality, inverse problems and nonlinear problems in solid mechanics

Effects of multi-scale roughness and frictional heating on solid body contact deformation

Kyriakos Komvopoulos

Department of Mechanical Engineering, University of California, Berkeley, CA 94720, USA

Available online 4 January 2008

Abstract

Solid body contact is restricted to a discrete number of randomly distributed microscopic areas resulting from the deformation of interacting surface protrusions (asperities). The deformation mode of these asperity contacts can be elastic, elastic–plastic, or fully plastic, depending on the local surface interference, asperity radius of curvature, coefficient of friction, and mechanical properties of the solid surfaces. Traditionally, the surface topography has been described by statistical models which rely on unrealistic simplifications of the shape, height, and size of the asperities. Such assumptions were avoided in contemporary contact mechanics analyses, which use fractal geometry to accomplish a surface topography description over a wide range of length scales. The main objective of this article is to provide an assessment of the role of multi-scale topography (roughness) and frictional heating in contact deformation of elastic–plastic solid bodies. Contact relationships, derived at the asperity level, which include the mechanical properties of surface layer and substrate medium, layer thickness, local surface interference, and equivalent asperity radius of curvature, are presented for different modes of deformation. These asperity-level relationships and a fractal model of the surface topography are incorporated into a numerical integration scheme to analyze multi-scale thermomechanical contact deformation over the entire real contact area of homogeneous and layered media possessing realistic surface topographies. ***To cite this article: K. Komvopoulos, C. R. Mecanique 336 (2008).***
© 2007 Académie des sciences. Published by Elsevier Masson SAS. All rights reserved.

Résumé

Effets de rugosité et de l'échauffement par frottement dans la déformation de contact de corps solides. Le contact entre corps solides n'a lieu que sur un nombre fini de zones microscopiques réparties aléatoirement, qui résultent de la déformation d'aspérités en interaction. Le mode de déformation de ces aspérités en contact peut être élastique, partiellement élastique et partiellement plastique, ou complètement plastique, suivant l'interférence locale des surfaces, le rayon de courbure des aspérités, le coefficient de frottement et les propriétés mécaniques des surfaces. Traditionnellement, la topographie des surfaces a été décrite à l'aide de modèles statistiques qui reposent sur des simplifications irréalistes de la forme, la hauteur et la taille des aspérités. Les analyses mécaniques actuelles du contact évitent de telles hypothèses en utilisant la géométrie fractale pour décrire la topographie des surfaces sur une large gamme d'échelles. Le but essentiel de cet article est d'examiner le rôle de la topographie multi-échelles (rugosité) et de l'échauffement par frottement dans la déformation de contact de corps solides élasto-plastiques. Des relations de contact obtenues à l'échelle des aspérités, qui font intervenir les propriétés mécaniques de la zone de surface et du substrat sous-jacent, l'épaisseur de la couche, l'interférence des surfaces et le rayon de courbure équivalent des aspérités, sont présentées pour différents modes de déformation. Ces relations d'origine microscopique, jointes à un modèle fractal de la topographie des surfaces, sont incorporées dans un schéma d'intégration numérique, afin d'analyser la déformation thermomécanique de contact de

E-mail address: kyriakos@me.berkeley.edu.

1631-0721/$ – see front matter © 2007 Académie des sciences. Published by Elsevier Masson SAS. All rights reserved.
doi:10.1016/j.crme.2007.11.005

la totalité de la zone de contact de milieux homogènes et laminés possédant des topographies de surface réalistes. ***Pour citer cet article : K. Komvopoulos, C. R. Mecanique 336 (2008).***
© 2007 Académie des sciences. Published by Elsevier Masson SAS. All rights reserved.

Keywords: Friction; Asperities; Fractal surfaces; Frictional heating; Homogeneous and layered media; Multi-scale contact deformation; Thermomechanical surface tractions

Mots-clés : Friction ; Aspérités ; Surfaces fractales ; Échauffement par frottement ; Milieux homogènes et laminés ; Déformation de contact multi-échelle ; Tractions surfaciques thermomécaniques

1. Introduction

Since the seminal contact analysis of elastic solids of revolution by Hertz [1], solid body contact has attracted significant research attention. Early studies were mainly focused on theoretical treatments of simplified contact problems, such as homogeneous elastic half-spaces [2] and layered media [3,4] in contact with smooth indenters, compression of an elastic layer on a rigid substrate by a frictionless stamp [5], normal contact of a cylinder with an elastic layered medium for the special cases of frictionless and rigid (perfect bonding) layer/substrate interface [6], and elastic contact of a cylinder with a layered medium [7]. A common contribution of these studies was the development of analytical solutions for the contact pressure distribution.

Advances in numerical methods and computational capabilities led to the incorporation of more realistic constitutive models in later contact mechanics studies. Contact analyses performed with the finite element method (FEM) showed that the accumulation of plastic deformation in indented elastic–plastic homogeneous media may result in contact pressure distributions that deviate significantly from that predicted by Hertz theory [8,9]. FEM analysis of repetitive indentation of an elastic–plastic half-space by a rigid sphere demonstrated a dependence of both contact pressure and subsurface plastic deformation on the number of indentation cycles and provided insight into elastic shakedown [10]. A significant decrease of the tensile stress arising in the substrate of a layered medium with a hard layer and intensification of both interfacial shear stress and surface tensile stress at the contact edge were observed in plane-strain indentation analyses performed with the FEM [11,12]. Effective hardness relationships for layered media possessing surface layers harder or softer than the substrate were extracted from FEM simulation results for an elastic–plastic layered medium indented by a rigid cone [13]. FEM analysis of a rigid sphere sliding over an elastic–plastic layered medium elucidated the effects of layer thickness and material properties, friction coefficient, and normal load on the contact pressure distribution and the evolution of subsurface stresses [14].

Despite important information regarding the role of the layer thickness and the material properties on the deformation behavior of layered media derived from previous contact mechanics analyses, the reported results are limited to smooth surface profiles and, therefore, are only applicable to macroscopic deformation behavior. Because even macroscopically smooth surfaces exhibit multi-scale roughness, high stress gradients in the vicinities of the asperity contacts are not captured in contact analyses of ideally smooth surfaces. In early studies dealing with the effect of surface roughness on contact deformation, the surface topography was approximated by a simple periodic waviness to enable analytical treatment. Elastic contact of a homogeneous half-space exhibiting sinusoidal surface waviness showed that both contact pressure and load versus contact length relationships deviated from corresponding Hertz solutions for small wavelengths (i.e., small asperity distances) [15–17]. In other elastic studies, the interaction of neighboring asperity contacts was found to greatly affect contact deformation [18,19]. An analysis of a rigid and smooth cylinder compressing an elastic cylinder with a wavy surface revealed local stress maxima below asperity contacts [20]. A significant roughness effect on the subsurface stress distributions up to depths that scaled with the asperity contact size was observed in an elastic analysis of lubricated contact interfaces [21].

The important effect of surface waviness on contact deformation demonstrated in previous studies provided impetus for the development of more realistic surface topography models. Randomly oriented elliptical contacts were found at contact interfaces with asperities modeled by elliptical paraboloids [22–24]. However, the statistical models of these studies do not account for multi-scale roughness and asperity interaction effects. The self-affinity property demonstrated by most surfaces led to the description of the interfacial topography by fractal geometry [25–27]. Contrary to traditional statistical models that are based on scale-dependent parameters for surface characterization, fractal geometry relies on scale-independent (fractal) surface topography parameters over a wide range of length scales where

the surface exhibits a particular fractal behavior. (Some surfaces may exhibit multi-fractal behavior, characterized by different fractal parameters over different wavelength ranges.) Consequently, fractal geometry was used in contemporary contact mechanics studies to examine deformation at the asperity level [28], normal and sliding contact of adhesive rough surfaces [29], elastic–plastic deformation of rough surfaces [30], adhesion of micromachine surfaces subjected to van der Waals, electrostatic, capillary, and asperity deformation forces [31], elastic–plastic contact of layered media possessing fractal topographies [32], temperature rise at sliding interfaces due to frictional heating [33, 34], development of stresses and strains below asperity contacts of elastic–plastic layered media [35], and sliding of a fractal surface against a homogeneous elastic half-space resulting in thermomechanical deformation [36].

The previous studies illustrate the important effects of surface topography on contact deformation of macroscopically smooth solid bodies. However, to analyze contact deformation of semi-infinite media, it is necessary to accurately describe the surface topography and account for asperity interaction effects over a wide range of length scales. The objectives of this article is to introduce basic aspects of multi-wavelength surface topography description, present contact deformation models derived at the asperity level, and elucidate the significance of multi-scale roughness and interfacial friction on deformation behavior of homogeneous and layered elastic–plastic media subjected to thermal and mechanical surface tractions.

2. Multi-scale surface topography description

Since surface topographies resemble a random process [37], surface power spectra obey a power-law relationship over a wide range of frequencies [38]. This is an inherent behavior of fractal geometry [27], characterized by intrinsic properties of continuity, nondifferentiability, and self-affinity, which can be satisfied by a complex function W of the form [39]

$$W(x) = \sum_{n=-\infty}^{\infty} \gamma^{(D-2)n}\left(1 - \mathrm{e}^{\mathrm{i}\gamma^n x}\right)\mathrm{e}^{\mathrm{i}\phi_n} \tag{1}$$

where x is a real parameter. A two-dimensional (2D) fractal profile $z(x)$ can be obtained as the real part of $W(x)$, i.e.,

$$z(x) = \mathrm{Re}\big[W(x)\big] = \sum_{n=-\infty}^{\infty} \gamma^{(D-2)n}\big[\cos\phi_n - \cos(\gamma^n x + \phi_n)\big] \tag{2}$$

where D is the fractal dimension ($1 < D < 2$ for 2D surface profiles), which is invariant in the frequency range throughout which the surface exhibits fractal behavior, n is a frequency index, ϕ_n is a random phase used to prevent the coincidence of different frequencies at any point of $z(x)$, and $\gamma(\gamma > 1)$ is a parameter that controls the density of frequencies in $z(x)$. Surface flatness and frequency distribution density considerations [40] suggest that $\gamma = 1.5$ is a physically reasonable value. Eq. (2) shows that $z(x)$ is a superposition of cosine functions with geometrically increasing frequencies. The mean square increment of $z(x)$, referred to as the structure function of $z(x)$, is defined as

$$S(\tau) = \big\langle\big[z(x+\tau, y) - z(x, y)\big]^2\big\rangle \tag{3}$$

where τ is termed the correlation length. The self-affine property is independent of x and can be expressed as

$$S(\gamma\tau) = \gamma^{2(2-D)}S(\tau) \tag{4}$$

Function $W(x)$ can be generalized to describe higher-dimensionality stochastic processes, while homogeneity and scaling (Eq. (4)) are preserved. Hence, a two-variable function can be used to represent a fractal surface that exhibits randomness in all directions (three-dimensional (3D) surface topography). Such a function is given by [41]

$$z(\rho, \theta) = \left(\frac{\ln\gamma}{M}\right)^{1/2} \sum_{m=1}^{M} A_m \sum_{n=-\infty}^{\infty} (k\gamma^n)^{(D-3)}\big\{\cos\phi_{m,n} - \cos\big[k\gamma^n\rho\cos(\theta - \alpha_m) + \phi_{m,n}\big]\big\} \tag{5}$$

where ρ and θ are the planar polar coordinates of a surface point of height z, which can be related to the planar coordinates x and y through $\rho = (x^2 + y^2)^{1/2}$ and $\theta = \tan^{-1}(y/x)$, D denotes again the fractal dimension ($2 < D < 3$ for 3D surfaces), and M is the number of superimposed ridges ($M = 1$ for 2D surfaces with cylindrical corrugations). Surface anisotropy depends on A_m, i.e., for isotropic surfaces $A_m = A$ for all m values, while for anisotropic surfaces

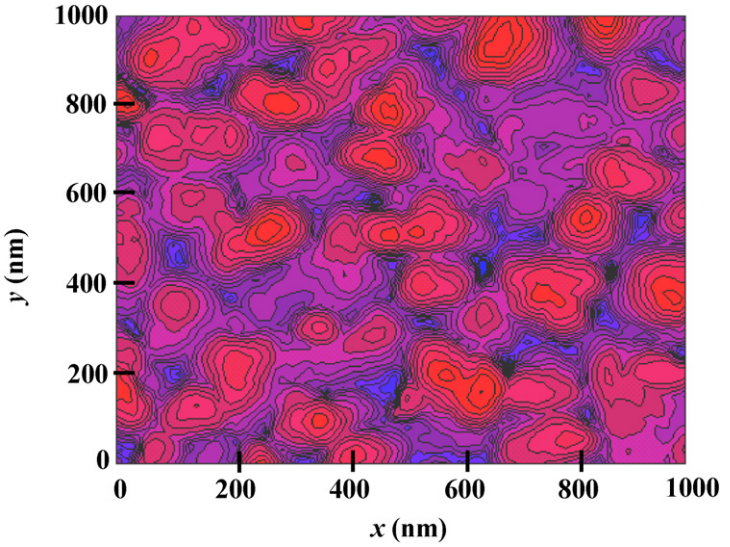

Fig. 1. Two-dimensional surface topography of a 3D fractal surface constructed from Eq. (7) for $G = 3.78 \times 10^{-3}$ nm and $D = 2.25$. The rms roughness of this surface is $\sigma = 13.6$ nm.

A_m is a function of m. An arbitrary angle α_m is used to offset the ridges in the azimuthal direction (for equally offset ridges, $\alpha_m = \pi m/M$) and a random number generator to uniformly distribute the values of random phase $\phi_{m,n}$ in the interval $[0, 2\pi]$. Wavenumber k and sample size L are related by $k = 2\pi/L$. In practice, the frequency index n is finite. Since the lowest frequency is $\omega_l = 1/L$, the lower limit of n can be set equal to zero. Because fractal geometry is not applicable at the atomic scale (breakdown of continuum description), the highest frequency is $\omega_h = 1/L_c$, where L_c is a cut-off wavelength, typically on the order of the interatomic distance. The upper limit of n is given by $n_{\max} = \text{int}[\log(L/L_c)/\log\gamma]$. The function of a 3D isotropic surface can be obtained by substituting the previous relationships of A_m, α_m, ρ, θ, k, and the lower and upper limits of n into Eq. (5), i.e.,

$$z(x,y) = A\left(\frac{L}{2\pi}\right)^{(3-D)}\left(\frac{\ln\gamma}{M}\right)^{1/2}\sum_{m=1}^{M}\sum_{n=0}^{n_{\max}}\gamma^{(D-3)n} \times\left\{\cos\phi_{m,n} - \cos\left[\frac{2\pi\gamma^n(x^2+y^2)^{1/2}}{L}\cos\left(\tan^{-1}\left(\frac{y}{x}\right) - \frac{\pi m}{M}\right) + \phi_{m,n}\right]\right\} \tag{6}$$

Substituting $A = 2\pi(2\pi/G)^{(2-D)}$ in Eq. (6) for consistency [40],

$$z(x,y) = L\left(\frac{G}{L}\right)^{(D-2)}\left(\frac{\ln\gamma}{M}\right)^{1/2}\sum_{m=1}^{M}\sum_{n=0}^{n_{\max}}\gamma^{(D-3)n}\left\{\cos\phi_{m,n} - \cos\left[\frac{2\pi\gamma^n(x^2+y^2)^{1/2}}{L}\cos\left(\tan^{-1}\left(\frac{y}{x}\right) - \frac{\pi m}{M}\right) + \phi_{m,n}\right]\right\} \tag{7}$$

Because G is a frequency independent scaling parameter, it is referred to as the fractal roughness. The only unknown parameters in Eq. (7) are the scale-independent fractal parameters G and D, which can be determined from a logarithmic plot of $S(\tau)$ [42]. Fig. 1 shows a plane view of a 3D fractal surface constructed from Eq. (7) using $G = 3.78 \times 10^{-3}$ nm and $D = 2.25$. The root-mean-square (rms) roughness of this surface is $\sigma = 13.6$ nm.

3. Distribution of asperity contacts

Fig. 2(a) shows a cross-sectional view of the contact interface of two layered media subjected to a normal load P. Because of the roughness effect, contact is confined at surface summits termed asperities. Fig. 2(b) shows an equivalent contact model, consisting of a rigid plane and a deformable rough surface with effective material properties

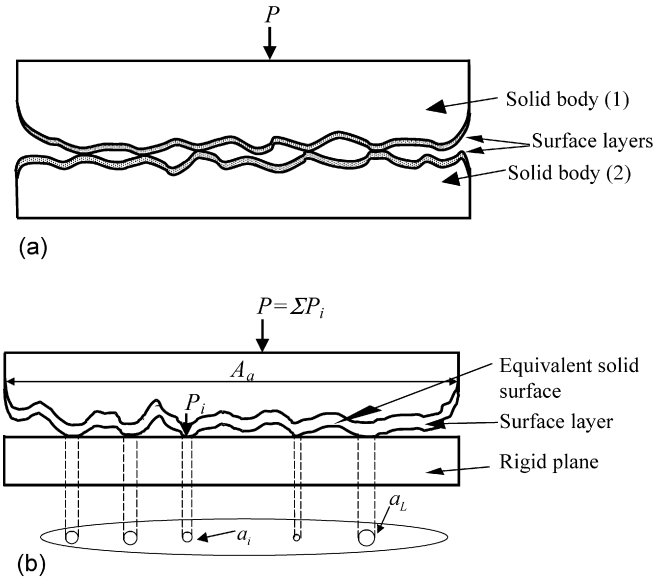

Fig. 2. (a) Cross-sectional view of the contact interface of two solid bodies with rough surfaces coated with a thin layer under a normal load and (b) equivalent contact model consisting of a rigid plane and a deformable solid body with effective (equivalent) material properties and surface topography showing the formation of individual asperity contacts.

and topography that are functions of those of each solid surface. The normal load P_i transmitted through the ith asperity contact depends on the projected contact area a_i (local curvature effect). The real contact area A_r is the summation of all the asperity contact areas obtained at a given global surface interference, with a_L denoting the largest asperity contact area. Hence, A_r is a small fraction of the apparent contact area A_a. For lightly loaded contact interfaces, such as those of hard disk drives and microelectromechanical systems, A_r/A_a typically varies in the range of 10^{-8}–10^{-6}, depending on contact load, topographies of contacting surfaces, and surface mechanical properties.

The development of normal and shear (friction) surface tractions and the resulting deformation depend strongly on the size and spatial distribution of the asperity contacts obtained at a given global surface interference. One of the most fundamental concepts in contact mechanics is the size distribution of the asperity contacts. A close similarity has been observed between surface asperity distributions and the Earth's island distribution. Fig. 3 shows the surface topography of a carbon-coated hard disk of rms roughness $\sigma \approx 0.2$ nm. Despite the extremely small roughness, the surface comprises asperity features that exhibit an island-like distribution. In light of this similarity, the power-law relationship of the island distribution used in geophysics [26,27] can be used to describe the number of truncated asperity contacts N of areas larger than a', i.e.,

$$N(a') = \left(\frac{a'_L}{a'}\right)^{(D-1)/2} \tag{8}$$

where a'_L is the largest truncated contact area. Hence, the 3D size distribution of the truncated asperity contacts can be written as

$$n(a') = -\frac{\mathrm{d}N(a')}{\mathrm{d}a'} = \frac{(D-1)}{2a'_L}\left(\frac{a'_L}{a'}\right)^{(D+1)/2} \tag{9}$$

The largest truncated contact area is related to the total truncated area of the 3D equivalent rough surface A' (determined numerically at a given global surface interference) and the fractal dimension D through the relationship

$$A' = \int_{a'_s}^{a'_L} a' n(a')\,\mathrm{d}a' = \frac{D-1}{3-D}\left[1 - \left(\frac{a'_s}{a'_L}\right)^{(3-D)/2}\right] a'_L \tag{10}$$

where a'_s is the smallest truncated contact area, which, for a continuum description, may be set equal to five or six times the lattice dimension. Eqs. (9) and (10) indicate that an approximate assessment of the size range $[a'_s, a'_L]$ and

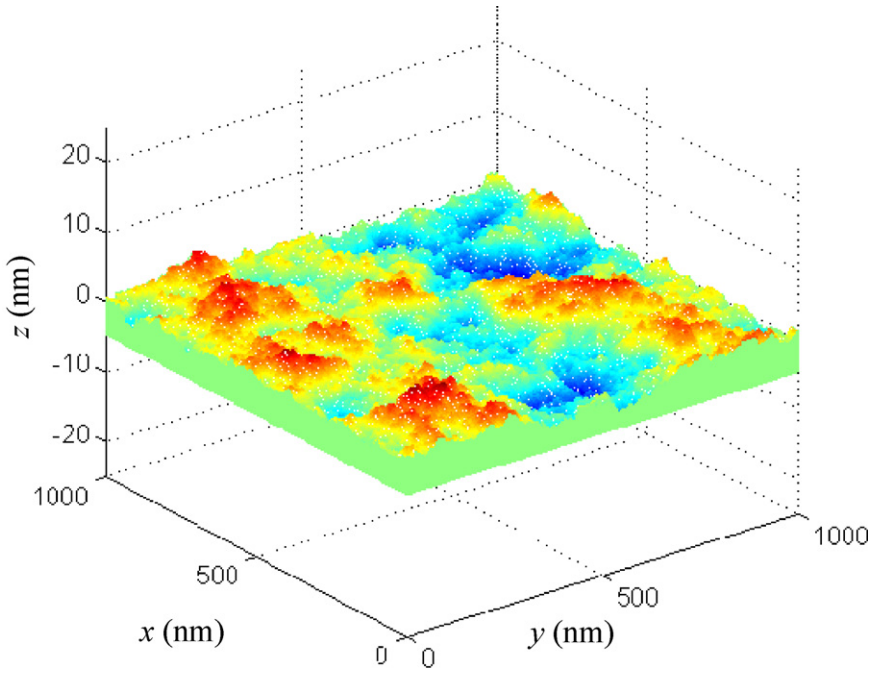

Fig. 3. Surface topography of a smooth ($\sigma \approx 0.2$ nm) carbon-coated magnetic rigid disk showing an island-like distribution of the surface asperities.

the spatial distribution of asperity contacts for a given global surface interference can be obtained from the truncated equivalent surface topography. The next step is to express the size of a truncated (undeformed) asperity contact in terms of the size of the corresponding deformed asperity contact and determine the associated mean contact pressure using asperity-based contact models.

4. Asperity contact deformation and effective material properties

As demonstrated by the 2D equivalent contact model shown schematically in Fig. 4(a), the truncation of the rough surface by a rigid plane produces several profile segments that contain asperity contacts of various sizes. This is a consequence of the multi-scale roughness effect on the conformation behavior of the contacting rough surfaces. The resulting asperity contacts may exhibit elastic, elastic–plastic, or fully plastic deformation, depending on the local surface interference, equivalent asperity radius, and effective material properties. For 3D surface description, the local surface interference at the ith asperity δ_i, shown in the cross-sectional view of the surface profile depicted in Fig. 4(b), and the equivalent asperity radius R_i are given by [30]

$$\delta_i = 2G^{(D-2)}(\ln\gamma)^{1/2}(2r_i')^{(3-D)} \tag{11}$$

$$R_i = \frac{(a_i')^{(D-1)/2}}{2^{(5-D)}\pi^{(D-1)/2}G^{(D-2)}(\ln\gamma)^{1/2}} \tag{12}$$

The mechanical properties of the deformable medium and the topography of the rigid rough surface are equivalent to those of the contacting solid bodies. In view of the dependence of the indentation hardness on yield strength [43], the equivalent (effective) yield strength of a layered medium σ_Y^* can be expressed in terms of the local surface interference as [13]

$$\sigma_Y^* = \sigma_{Y,s} + (\sigma_{Y,l} - \sigma_{Y,s})\exp\left[-\left(\frac{\delta_i}{h}\right)\left(\frac{E_s}{E_l}\right)^{1/2}\right] \tag{13}$$

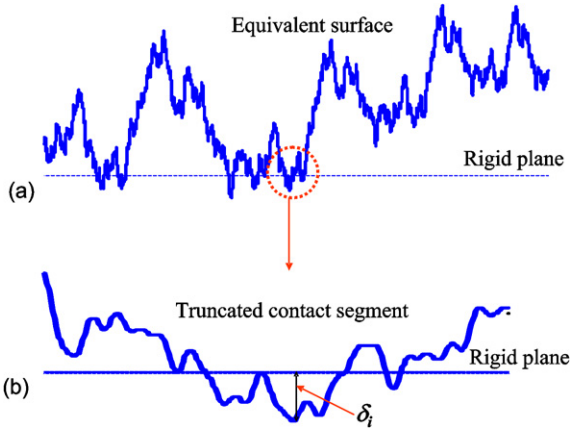

Fig. 4. (a) Truncation of equivalent 2D fractal surface (or 3D isotropic fractal surface) by a rigid plane resulting in several contact segments and (b) close-up view of a contact segment showing the local interference at an individual asperity contact.

where h is the layer thickness, E is the elastic modulus, and subscripts l and s denote layer and substrate material properties, respectively. The equivalent (effective) elastic modulus E^* can be related to the local surface interference through the relationship [44]

$$E^* = \left[\left(1 - \exp\left[-\alpha h/r_i\sqrt{\pi}\,\right]\right)\left(\frac{1-\nu_l^2}{E_l}\right) + \exp\left[-\alpha h/r_i\sqrt{\pi}\,\right]\left(\frac{1-\nu_s^2}{E_s}\right)\right]^{-1} \tag{14}$$

where α is a numerically determined geometrical factor that depends on the indenter shape [44], r_i is the radius of the asperity contact area a_i at the particular local surface interference and ν is the Poisson's ratio.

Using Eqs. (11), (13), and (14), the representative strain ε_R at an asperity contact of truncated radius r_i' and local surface interference δ_i can be defined as

$$\varepsilon_R = \frac{E^*\delta_i}{\sigma_Y^* r_i'} \tag{15}$$

Eq. (15) shows that the deformation behavior at the asperity level is controlled by the local surface interference. It is noted that ε_R is also a function of the equivalent asperity radius (Eq. (12)). The asperity deformation can be elastic, elastic–plastic, or fully plastic, depending on the representative strain (Eq. (15)). Relationships for the mean contact pressure $p_{m,i}$ and the real contact area a_i of the deformed ith asperity are given below for different deformation modes [32].

- Elastic deformation ($\varepsilon_R < 1.78$),

$$p_{m,i} = \frac{4\sqrt{2}}{3\pi}\varepsilon_R\sigma_Y^*, \qquad a_i = \frac{a_i'}{2} = \frac{\pi(r_i')^2}{2} \tag{16}$$

- Elastic–plastic deformation ($1.78 \leqslant \varepsilon_R < 21$),

$$p_{m,i} = [0.70\ln\varepsilon_R + 0.66]\sigma_Y^*, \qquad a_i = \frac{\pi(r_i')^2}{0.05(\ln\varepsilon_R)^2 - 0.57\ln\varepsilon_R + 2.41} \tag{17}$$

- Fully plastic deformation ($21 \leqslant \varepsilon_R \leqslant 400$),

$$p_{m,i} = 2.9\sigma_Y^*, \qquad a_i = \frac{\pi(r_i')^2}{0.05(\ln\varepsilon_R)^2 - 0.57\ln\varepsilon_R + 2.41} \tag{18}$$

- Fully plastic deformation ($400 < \varepsilon_R$),

$$p_{m,i} = 2.9\sigma_Y^*, \qquad a_i = \frac{\pi(r_i')^2}{0.71} \tag{19}$$

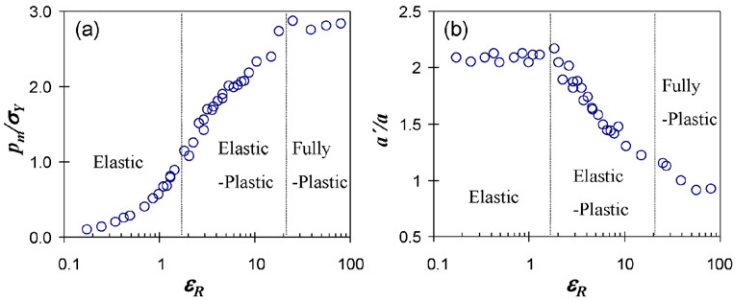

Fig. 5. (a) Mean contact pressure and (b) truncated-to-real contact area ratio versus representative strain [32].

The physical meaning of the previous contact relationships is demonstrated in Fig. 5. It can be seen that the asperity mean contact pressure and contact area are strong functions of the representative strain, which depends on the equivalent elastic and plastic material properties (Eqs. (13) and (14)), local surface interference (Eq. (11)), and truncated contact radius (or equivalent asperity radius of curvature (Eq. (12)). Fig. 5 also shows the transition from purely elastic to elastic–plastic, and then, to fully-plastic deformation with the increase of ε_R. An iteration procedure is needed to determine the equivalent elastic modulus because of its dependence on the unknown real contact radius (Eq. (14)). A plausible approach is to initially assume that $r_i = r_i'$ and calculate the new real contact radius using the appropriate contact area relationship (Eqs. (16)–(19)), depending on the value of ε_R calculated for the assumed r_i' value (Eq. (15)). This iteration procedure can be repeated until the change in the real contact radius of the particular asperity reaches a specified small tolerance.

5. Contact stress analysis

The contact relationships presented in the previous section can be implemented in contact stress analyses of half-space media possessing fractal surface topographies. Without loss of generality, the mathematical treatments of the mechanical and thermomechanical deformation of elastic half-space media [36,45] presented in this section are for 2D fractal surfaces. A similar approach can be adopted for 3D elastic fractal surfaces. For elastic–plastic deformation, analytical approaches involving multi-scale roughness effects are extremely cumbersome. Therefore, numerical techniques such as the FEM must be used to determine the stresses and strains in contacting elastic–plastic bodies (e.g., [35,36]).

5.1. Mechanical stresses

The stress field in a layered elastic medium in contact with a rough surface can be obtained by the superposition of the stress fields generated by normal and shear tractions with triangular distributions of width $2c$ (used to approximate the contact pressure and shear stress distributions at each asperity contact) and another superposition of the stress fields of all the asperity contacts established at a given global surface interface [45]. The mechanical stresses can be obtained from an Airy stress function Φ that satisfies the biharmonic equation $\nabla^4\Phi = 0$. Hence,

$$\sigma_{zz} = \frac{\partial^2\Phi}{\partial x^2}, \qquad \sigma_{xx} = \frac{\partial^2\Phi}{\partial z^2}, \qquad \sigma_{zx} = -\frac{\partial^2\Phi}{\partial z\partial x} \tag{20}$$

For triangular normal and shear stress distributions of width $2c$ at the contact interface, the boundary conditions at the layer surface ($z = 0$) and the stress and displacement continuity conditions at the layer/substrate interface ($z = h$) can be expressed as [45]

$$\sigma_{zz}^{(l)}(x,0) = \begin{cases} -p_0(1-|x|/c), & |x| \leqslant c \\ 0, & |x| > c \end{cases}$$

$$\sigma_{zx}^{(l)}(x,0) = \begin{cases} -q_0(1-|x|/c), & |x| \leqslant c \\ 0, & |x| > c \end{cases}$$

$$\sigma_{zx}^{(l)}(x,h) = \sigma_{zx}^{(s)}(x,0)$$

$$\sigma_{zz}^{(l)}(x,h) = \sigma_{zz}^{(s)}(x,0)$$
$$u^{(l)}(x,h) = u^{(s)}(x,0)$$
$$w^{(l)}(x,h) = w^{(s)}(x,0) \tag{21}$$

where superscripts l and s refer to the layer and the substrate media, p_0 and q_0 denote the maximum normal and shear stresses ($q_0 = fp_0$, where f is the coefficient of friction) in associated triangular stress distributions of width $2c$, and u and w are the displacements in the x and z directions, respectively. The Fourier transform of function Φ with respect to x is given by

$$\bar{\Phi} = \int_{-\infty}^{+\infty} \Phi(x,z)\mathrm{e}^{\mathrm{i}\omega x}\,\mathrm{d}x \tag{22}$$

For Φ to satisfy $\nabla^4\Phi = 0$ and to produce finite stresses at infinity [45]:

$$\bar{\Phi}^{(l)} = (A + Bz_l)\mathrm{e}^{-|\omega|z_l} + (C + Dz_l)\mathrm{e}^{|\omega|z_l}$$
$$\bar{\Phi}^{(s)} = (E + Fz_s)\mathrm{e}^{-|\omega|z_s} \tag{23}$$

where $\bar{\Phi}^{(l)}$ and $\bar{\Phi}^{(s)}$ are solutions of $\bar{\Phi}$ in the layer and substrate media, respectively, and z_l and z_s are corresponding z coordinates ($z_l = 0$ at the layer surface and $z_s = 0$ at the layer/substrate interface). Eqs. (21) represent a set of six coupled equations, including the coefficients in Eq. (23) and the Fourier transforms of surface traction distributions $p(x,z)$ and $q(x,z)$. After the determination of $\bar{\Phi}$, the stresses can be calculated from Eqs. (20) using the inverse transform of $\bar{\Phi}$. Hence, the stress at a point (x,z) in the layered medium can be written as [45]

$$\sigma(x,z) = \sum_{i=1}^{N}\sum_{j=1}^{M_i-1} \sigma|_i^j(x,z) \tag{24}$$

where M_i is the total number of grid nodes along the width of the ith asperity contact (grit size $= 2c$), N is the number of asperity contacts at a given global surface interference (Eq. (8)), and $\sigma|_i^j$ is the stress at the ith asperity contact due to the jth triangular distributions of normal and shear tractions.

Figs. 6(a) and 6(b) show distributions of the first principal stress σ_1 and the von Mises equivalent stress $\sigma_M = (\frac{3}{2}S_{ij}S_{ij})^{1/2}$ (where S_{ij} is the deviatoric stress tensor given by $S_{ij} = \sigma_{ij} - \sigma_m\delta_{ij}$, in which σ_{ij} is the stress tensor, σ_m is the mean (hydrostatic) stress ($\sigma_m = \sigma_{ii}/3$), and δ_{ij} is Kronecker's delta) in an elastic layered medium with a layer stiffer than the substrate ($E_l/E_s = 4$). Corresponding contact segments of the rigid (equivalent) fractal profile are also shown at the top of the figure. The σ_1 stress contours (Fig. 6(a)) reveal that tensile stresses occur only in the layer. It is noted that maximum tensile stresses arise only at the layer surface and the layer/substrate interface, implying that crack initiation in layered media with very stiff (hard) surface layers is most likely to occur either at the layer surface or at the layer/substrate interface. Fig. 6(b) shows that the maximum σ_M stresses are also confined within the stiff layer. In addition, the σ_M stress exhibits significant discontinuities at the layer/substrate interface, and the effect of asperity interaction on the stresses is especially pronounced below contact segment 2. Thus, the stiff layer relaxes the substrate from high stresses at the expense of steep stress/strain gradients in the vicinities of asperity contacts. This is a consequence of the increase of the surface penetration resistance of the layered medium due to the stiff layer.

5.2. Thermomechanical stresses

The average shear stress at the ith asperity contact $\tau_{m,i}$ can be expressed in terms of corresponding mean contact pressure $p_{m,i}$ and local coefficient of friction f as

$$\tau_{m,i} = fp_{m,i} \tag{25}$$

Eq. (25) can be used in conjunction with the mean contact pressure relationships (Eqs. (16)–(19)) to obtain shear stress relationships at the asperity level. In this approach, it is presumed that the friction effect on the contact area relationships is secondary. This assumption implies insignificant junction growth and relatively low-friction sliding conditions (e.g., $f \leqslant 0.5$).

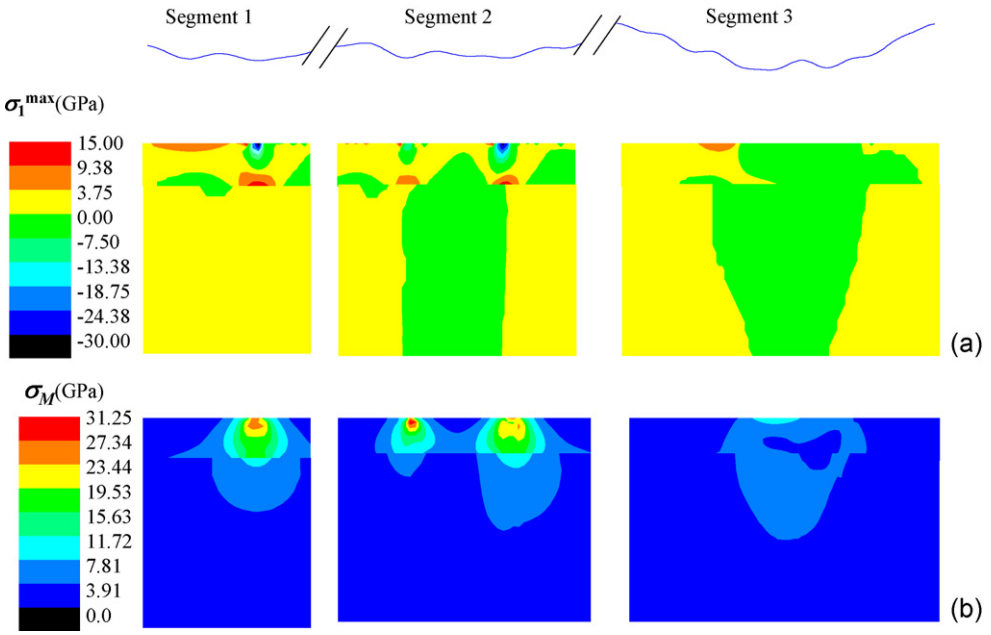

Fig. 6. Variation of (a) first principal stress σ_1 and (b) von Mises equivalent stress σ_M in an elastic layered medium ($E_l/E_s = 4$, $h/\sigma = 0.23$, $D = 1.34$, $G = 9.46 \times 10^{-4}$ nm, $\delta_{max}/\sigma = 0.25$, and $f = 0.5$) [45].

Friction induced surface heating produces thermal spikes (flash temperatures) and thermal stresses. Knowledge of the evolution of thermoelastic stresses in contacting solid bodies is critical to failure analysis because of the synergistic thermal and mechanical effects. Early studies provided closed-form solutions for the flash temperature and the temperature rise at the surface of a homogeneous half-space due to a moving source of uniform heat flux [46,47]. These primitive analyses provided impetus for further analytical studies, which revealed the occurrence of predominantly compressive surface stresses in the case of a fast moving heat source [48] and the development of a maximum tensile thermal stress slightly below the trailing edge of the contact region, extending to a depth controlled by the Peclet number [49].

To analyze the effect of frictional heating on contact deformation, it is necessary to consider the interdependence of mechanical and thermal stresses. This is because frictional heating affects the real contact area and, in turn, the contact pressure distribution due to the thermal expansion. Such changes in the asperity contact area influence local heat generation and conduction, resulting in fully coupled thermal and mechanical stresses. The interdependence of thermal and mechanical stresses has been considered in recent numerical and analytical studies of thermomechanical contact deformation of elastic–plastic layered media with smooth, patterned, and fractal surfaces [36,50,51]. The heat flux density due to frictional heating at the ith asperity contact can be expressed as

$$Q_i = \psi \tau_{m,i} V = \psi f p_{m,i} V \tag{26}$$

where ψ is the fraction of mechanical work dissipated as heat. It has been argued [52] that all the energy dissipated in a frictional contact is converted to heat (i.e., $\psi = 1.0$). Hence, the rigid (equivalent) rough surface can be assumed to be adiabatic, resulting in heat conduction only into the elastic half-space.

For a homogeneous elastic half-space with a 2D fractal surface profile, the normal displacement at an asperity contact w can be obtained as the sum of the normal surface displacements due to normal stress (contact pressure) w^N, shear stress w^S, and thermoelastic distortion w^T [36],

$$w = w^N + w^S + w^T \tag{27}$$

where w^N, w^S, and w^T are given by [53,54]

$$w^N = -\frac{(1-\nu^2)}{2\pi E}\frac{p_0}{b}\left\{(x+b)^2 \ln\left(\frac{x+b}{b}\right)^2 + (x-b)^2 \ln\left(\frac{x-b}{b}\right)^2 - 2x^2 \ln\left(\frac{x}{b}\right)^2\right\} + C \tag{28a}$$

$$w^S = \begin{cases} \dfrac{(1-2\nu)(1+\nu)}{E}\dfrac{q_0}{b}x\left(b-\dfrac{|x|}{2}\right), & |x| \leqslant b \\ \dfrac{(1-2\nu)(1+\nu)}{E}\dfrac{q_0 b}{2}, & x > b \\ -\dfrac{(1-2\nu)(1+\nu)}{E}\dfrac{q_0 b}{2}, & x < -b \end{cases} \tag{28b}$$

$$w^T = \begin{cases} \lambda, & \xi \leqslant -1 \\ \lambda\int_{-1}^{1}(1-|\eta|)\mathrm{e}^{-Pe(\xi-\eta)}I_0\big[Pe(\xi-\eta)\big]\,\mathrm{d}\eta, & \xi \geqslant 1 \\ \lambda\Big\{\int_{-1}^{\xi}(1-|\eta|)\mathrm{e}^{-Pe(\xi-\eta)}I_0\big[Pe(\xi-\eta)\big]\,\mathrm{d}\eta + \frac{1}{2} - \xi + \frac{1}{2}\xi^2\,\mathrm{sgn}(\xi)\Big\}, & -1 \leqslant \xi \leqslant 1 \end{cases} \tag{28c}$$

where b is the width of triangular segments used to approximate the contact pressure distribution at the asperity contacts, C is a constant determined from a reference point on the z axis at a finite distance from the surface, Pe is the Peclet number ($Pe = Vb/2\kappa$), I_0 is the modified zero-order Bessel function of the first kind, and ξ, ζ, η, and λ are dimensionless parameters defined as

$$\xi = \frac{x}{b}, \quad \zeta = \frac{z}{b}, \quad \eta = \frac{x+Vt}{b}, \quad \text{and} \quad \lambda = -\frac{\alpha Q_0(1+\nu)b^2}{\rho c\kappa\, Pe}$$

where Q_0 ($= \psi f p_0 V$) is the peak heat flux, (x, z) is the coordinate system attached to the moving fractal surface, V is the sliding velocity, t is the time, and α, ρ, c, and κ are the thermal expansion, mass density, specific heat, and thermal diffusivity, respectively.

The total surface displacement w can be obtained by summing up the displacements at each triangular element of width b (Eqs. (28a)–(28c)) and then integrating over the entire real contact area [36], i.e.,

$$w(x) = \sum_{i=1}^{N}\sum_{j=1}^{M_i-1}\big[w^N|_i^j(x) + w^S|_i^j(x) + w^T|_i^j(x)\big] \tag{29}$$

where N is the total number of asperity contacts (Eq. (8)), M_i is the total number of segments of width b in the ith asperity contact (i.e., grit size $= b$), and $w^N|_i^j$, $w^S|_i^j$, and $w^T|_i^j$ are the normal surface displacements at the ith asperity contact due to the jth triangular distributions of contact pressure, shear stress, and thermal distortion, respectively. Eq. (29) can be expressed in matrix form as $\boldsymbol{W} = \boldsymbol{C}\,\boldsymbol{P}$, where $\boldsymbol{W}$ is the matrix of normal surface displacements, $\boldsymbol{P}$ is the contact pressure matrix, and $\boldsymbol{C}$ is a square and symmetric matrix referred to as the influence coefficient matrix. This matrix relationship can be solved by a procedure which uses the matrix inversion method [36].

The temperature rise ΔT due to a surface heat source with a triangular distribution of width b is given by [36]

$$\Delta T = \frac{Q_0 b}{\pi k}\int_{-1}^{1}(1-|\eta|)\mathrm{e}^{-Pe(\xi+\eta)}K_0\big\{Pe\big[(\xi+\eta)^2+\zeta^2\big]^{1/2}\big\}\,\mathrm{d}\eta \tag{30}$$

where k is the thermal conductivity and K_0 is the modified zero-order Bessel function of the second kind. Therefore, the temperature rise at a point (x, z) is given by [36]

$$\Delta T(x,z) = \sum_{i=1}^{N}\sum_{j=1}^{M_i-1}\Delta T|_i^j(x,z) \tag{31}$$

where $\Delta T|_i^j(x,z)$ is the temperature rise at the ith asperity contact due to the jth triangular distribution of heat flux.

The thermal stresses in an elastic half-space due to a moving heat source of triangular distribution of width b are given by [36]

$$\hat{\sigma}_{xx}^T = \frac{E\alpha\hat{T}_0}{(1-\nu)\beta}\big\{\big[2(b_2+b_1\mathrm{i})\,\mathrm{sgn}(\omega) - \omega\mathrm{i} - \omega z\big(b_2+b_1\mathrm{i}-|\omega|\mathrm{i}\big)\big]\mathrm{e}^{-|\omega|z} - (\beta+\omega\mathrm{i})\mathrm{e}^{(b_2\mathrm{i}-b_1)z}\big\} \tag{32a}$$

$$\hat{\sigma}_{zz}^T = \frac{E\alpha\hat{T}_0}{(1-\nu)\beta}\big\{\big[-\omega\mathrm{i} + \omega z\big(b_2+b_1\mathrm{i}-|\omega|\mathrm{i}\big)\big]\mathrm{e}^{-|\omega|z} + \omega\mathrm{i}\mathrm{e}^{(b_2\mathrm{i}-b_1)z}\big\} \tag{32b}$$

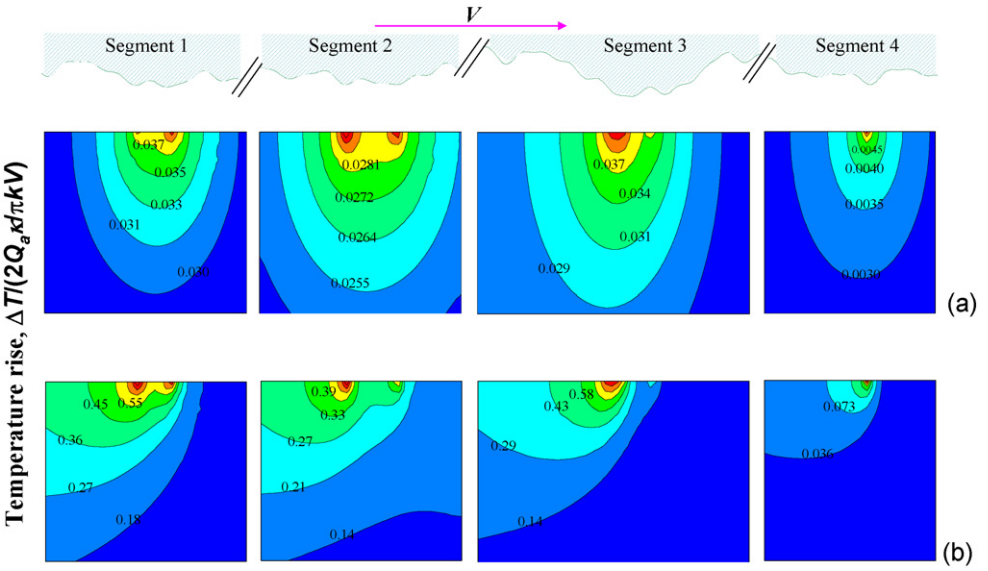

Fig. 7. Effect of Peclet number on the variation of the temperature rise ΔT in an elastic homogeneous medium ($D = 1.44$, $G = 9.46 \times 10^{-4}$ nm, $\delta_{\max}/\sigma = 0.25$, and $f = 0.5$): (a) $Pe = 0.06$ and (b) $Pe = 5.58$ [36].

$$\hat{\sigma}^T_{zx} = \frac{E\alpha\hat{T}_0}{(1-\nu)\beta}\left\{\left[b_2\mathrm{i} - b_1 - |\omega|z\left(b_2\mathrm{i} - b_1 + |\omega|\right)\right]\mathrm{e}^{-|\omega|z} + (b_1 - a\mathrm{i})\mathrm{e}^{(b_2\mathrm{i}-b_1)z}\right\} \tag{32c}$$

where $\mathrm{i} = \sqrt{-1}$, $\beta = V/\kappa$, $b_1 = \left(\frac{\omega^2+\omega\sqrt{\omega^2+\beta^2}}{2}\right)^{1/2}$, $b_2 = \frac{\beta\omega}{2b_1}$, and $\hat{T}_0 = \frac{2[1-\cos(b_2\omega)]}{b_2\omega^2 k(b_1-b_2\mathrm{i})}$.

The stresses due to frictional heating can be obtained from the inverse Fourier transform of the numerical solution,

$$\sigma^T(x,z) = \int_{-\infty}^{+\infty} \hat{\sigma}^T(\omega,z)\mathrm{e}^{\mathrm{i}\omega x}\mathrm{d}\omega \tag{33}$$

where σ^T and $\hat{\sigma}^T$ are thermal stress components in spatial and frequency domains, respectively. Hence, the stress at a point (x, z) in the half-space medium can be expressed as [36]

$$\sigma(x,z) = \sum_{i=1}^{N}\sum_{j=1}^{M_i-1}\left[\sigma^N|_i^j(x,z) + \sigma^S|_i^j(x,z) + \sigma^T|_i^j(x,z)\right] \tag{34}$$

where $\sigma^N|_i^j$, $\sigma^S|_i^j$, and $\sigma^T|_i^j$ are the stresses at the ith asperity contact due to the jth triangular distributions of contact pressure, shear traction, and surface heat flux, respectively.

Fig. 7 shows temperature rise contours in a semi-infinite elastic medium sliding against a 2D fractal profile ($D = 1.44$ and $G = 9.46 \times 10^{-4}$ nm) for relatively low and high Peclet numbers and $f = 0.5$. The temperature rise ΔT was normalized by $2Q_a\kappa/\pi kV$, where Q_a is the average heat flux rate across the entire contact region (i.e., total heat flux divided by the real contact area). Contact segments of the sliding rough surface are shown at the top of the figure. As expected, the highest temperature rises always occur at the surface regardless of Peclet number. In addition, significantly higher temperatures and marked changes in the temperature distributions below each contact segment can be seen for $Pe = 6$ (Fig. 7(b)) compared to the fairly symmetric temperature fields obtained for $Pe = 0.06$ (Fig. 7(a)).

The increase of the surface temperature with the Peclet number led to intensification of the thermomechanical stresses. Figs. 8(a) and 8(b) show a comparison between elastic ($Pe = 0$) and thermoelastic ($Pe = 54$) σ_M stress distributions in the same subsurface regions as those shown in Fig. 7. It can be observed that frictional heating increased the stresses, especially below asperity contacts in segments 1 and 2 where thermoelastic deformation promoted interaction of the stress fields of neighboring asperity contacts. The increase of the maximum σ_M stress at the surface as a result of frictional heating is equal to ~23%. These analytical results are supported by FEM simulations that show a strong effect of frictional heating on the location of the maximum σ_M stress [50].

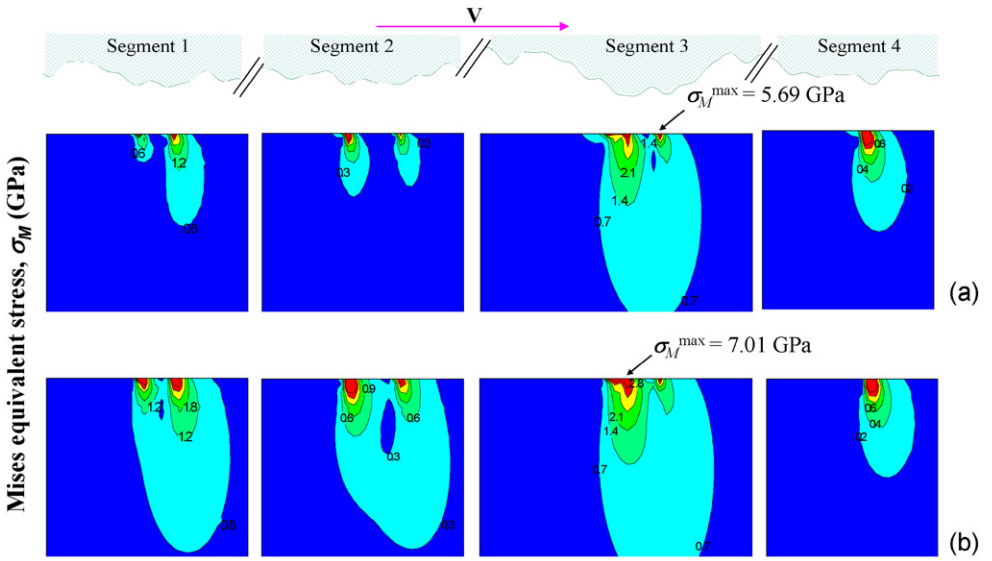

Fig. 8. Effect of Peclet number on the variation of the von Mises equivalent stress σ_M in an elastic homogeneous medium ($D = 1.44$, $G = 9.46 \times 10^{-4}$ nm, $\delta_{max}/\sigma = 0.25$, and $f = 0.5$): (a) $Pe = 0$ (elastic) and (b) $Pe = 54$ (thermoelastic) [36].

6. Summary

An analysis of the effects of multi-scale roughness and frictional heating on solid body contact deformation was presented for homogeneous and layered half-space media with surface topographies exhibiting fractal behavior. Theoretical and numerical analyses leading to asperity contact relationships, equivalent contact models of the interfacial topography and mechanical properties of the contacting solids, and mechanical/thermomechanical stress analyses were introduced to establish a generalized mechanics treatment of multi-scale contact deformation of real solid surfaces. Numerical results demonstrated the effectiveness of the present analysis to account for asperity interactions over a wide range of length scales and to provide solutions for complex stress and deformation fields in solid bodies with realistic surface topographies subjected to thermomechanical surface tractions.

References

[1] H. Hertz, Über die berührung fester elastischer körper (On the contact of elastic solids), J. Reine Angewandte Mathematik 92 (1882) 156–171.
[2] Y.-O. Tu, A numerical solution for an axially symmetric contact problem, J. Appl. Mech. 34 (1967) 283–286.
[3] M. Hannah, Contact stress and deformation in a thin elastic layer, Quart. J. Mech. Appl. Math. 4 (1951) 94–105.
[4] D.M. Burmister, The general theory of stresses and displacements in layered systems, J. Appl. Phys. 16 (1945) 89–94.
[5] V.M. Aleksandrov, V.A. Babeshko, V.A. Kucherov, Contact problems for an elastic layer of slight thickness, J. Appl. Math. Mech. (PMM) 30 (1966) 124–142.
[6] Y.C. Pao, T.-S. Wu, Y.P. Chiu, Bounds on the maximum contact stress of an indented elastic layer, J. Appl. Mech. 38 (1971) 608–614.
[7] P.K. Gupta, J.A. Walowit, Contact stresses between an elastic cylinder and a layered elastic solid, J. Lubr. Technol. 96 (1974) 250–257.
[8] G. Dumas, C.N. Baronet, Elastoplastic indentation of a half-space by an infinitely long rigid circular cylinder, Int. J. Mech. Sci. 18 (1971) 519–530.
[9] G.B. Sinclair, P.S. Follansbee, K.L. Johnson, Quasi-static normal indentation of an elasto-plastic half-space by a rigid sphere—II. Results, Int. J. Solids Struct. 21 (1985) 865–888.
[10] E.R. Kral, K. Komvopoulos, D.B. Bogy, Elastic–plastic finite element analysis of repeated indentation of a half-space by a rigid sphere, J. Appl. Mech. 60 (1993) 829–841.
[11] K. Komvopoulos, Finite element analysis of a layered elastic solid in normal contact with a rigid surface, J. Tribol. 110 (1988) 477–485.
[12] K. Komvopoulos, Elastic–plastic finite element analysis of indented layered media, J. Tribol. 111 (1989) 430–439.
[13] A.K. Bhattacharya, W.D. Nix, Analysis of elastic and plastic deformation associated with indentation testing of thin films on substrates, Int. J. Solids Struct. 24 (1988) 1287–1298.
[14] E.R. Kral, K. Komvopoulos, Three-dimensional finite element analysis of surface deformation and stresses in an elastic–plastic layered medium subjected to indentation and sliding contact loading, J. Appl. Mech. 63 (1996) 365–375.
[15] J. Dundurs, K.C. Tsai, L.M. Keer, Contact between elastic bodies with wavy surfaces, J. Elast. 3 (1973) 109–115.
[16] M.N. Webster, R.S. Sayles, A numerical model for the elastic frictionless contact of real rough surfaces, J. Tribol. 108 (1986) 314–320.

[17] J. Seabra, D. Berthe, Influence of surface waviness and roughness on the normal pressure distribution in the Hertzian contact, J. Tribol. 109 (1987) 462–470.
[18] D. Berthe, Ph. Vergne, An elastic approach to rough contact with asperity interactions, Wear 117 (1987) 211–222.
[19] K. Komvopoulos, D.-H. Choi, Elastic finite element analysis of multi-asperity contacts, J. Tribol. 114 (1992) 823–831.
[20] D. Nowell, D.A. Hills, Hertzian contact of ground surfaces, J. Tribol. 111 (1989) 175–179.
[21] E. Ioannides, J.C. Kuijpers, Elastic stresses below asperities in lubricated contacts, J. Tribol. 108 (1986) 394–402.
[22] A.W. Bush, R.D. Gibson, T.R. Thomas, The elastic contact of a rough surface, Wear 35 (1975) 87–111.
[23] A.W. Bush, R.D. Gibson, G.P. Keogh, Strongly anisotropic rough surfaces, J. Lubr. Technol. 101 (1979) 15–20.
[24] J.I. McCool, Predicting microfracture in ceramics via a microcontact model, J. Tribol. 108 (1986) 380–386.
[25] B.B. Mandelbrot, How long is the coast of Britain? Statistical self-similarity and fractional dimension, Science 156 (1967) 636–638.
[26] B.B. Mandelbrot, Stochastic models for the Earth's relief, the shape and the fractal dimension of the coastlines, and the number-area rule for islands, Proc. Natl. Acad. Sci. 72 (1975) 3825–3828.
[27] B.B. Mandelbrot, The Fractal Geometry of Nature, Freeman, New York, 1983, pp. 1–83 and 116–118.
[28] A. Majumdar, B. Bhushan, Fractal model of elastic–plastic contact between rough surfaces, J. Tribol. 113 (1991) 1–11.
[29] P. Sahoo, S.K. Roy Chowdhury, A fractal analysis of adhesion at the contact between rough solids, Proc. Inst. Mech. Eng. Part J: J. Eng. Tribol. 210 (1996) 269–279.
[30] W. Yan, K. Komvopoulos, Contact analysis of elastic–plastic fractal surfaces, J. Appl. Phys. 84 (1998) 3617–3624.
[31] K. Komvopoulos, W. Yan, Three-dimensional elastic–plastic fractal analysis of surface adhesion in microelectromechanical systems, J. Tribol. 120 (1998) 808–813.
[32] K. Komvopoulos, N. Ye, Three-dimensional contact analysis of elastic–plastic layered media with fractal surface topographies, J. Tribol. 123 (2001) 632–640.
[33] S. Wang, K. Komvopoulos, A fractal theory of the interfacial temperature distribution in the slow sliding regime: Part I—Elastic contact and heat transfer analysis, J. Tribol. 116 (1994) 812–823.
[34] S. Wang, K. Komvopoulos, A fractal theory of the interfacial temperature distribution in the slow sliding regime: Part II—Multiple domains, elastoplastic contacts and applications, J. Tribol. 116 (1994) 824–832.
[35] K. Komvopoulos, N. Ye, Elastic–plastic finite element analysis for the head-disk interface with fractal topography description, J. Tribol. 124 (2002) 775–784.
[36] Z.-Q. Gong, K. Komvopoulos, Thermomechanical analysis of semi-infinite solid in sliding contact with a fractal surface, J. Tribol. 127 (2005) 331–342.
[37] R.S. Sayles, T.R. Thomas, Surface topography as a nonstationary random process, Nature 271 (1978) 431–434.
[38] A. Majumdar, C.L. Tien, Fractal characterization and simulation of rough surfaces, Wear 136 (1990) 313–327.
[39] M.V. Berry, Z.V. Lewis, On the Weierstrass–Mandelbrot fractal function, Proc. Roy. Soc. London, Ser. A 370 (1980) 459–484.
[40] K. Komvopoulos, W. Yan, A fractal analysis of stiction in microelectromechanical systems, J. Tribol. 119 (1997) 391–400.
[41] M. Ausloos, D.H. Berman, A multivariate Weierstrass–Mandelbrot function, Proc. Roy. Soc. London, Ser. A 400 (1985) 331–350.
[42] K. Komvopoulos, Surface engineering and microtribology for microelectromechanical systems, Wear 200 (1996) 305–327.
[43] D. Tabor, The hardness of solids, Rev. Phys. Technol. 1 (1970) 145–179.
[44] R.B. King, Elastic analysis of some punch problems for a layered medium, Int. J. Solids Struct. 23 (1987) 1657–1664.
[45] K. Komvopoulos, Z.-Q. Gong, Stress analysis of a layered elastic solid in contact with a rough surface exhibiting fractal behavior, Int. J. Solids Struct. 44 (2007) 2109–2129.
[46] H. Blok, Theoretical study of temperature rise at surfaces of actual contact under oiliness lubricating conditions, in: Proc. General Discussion on Lubrication and Lubricants, vol. 2, Inst. Mech. Eng. (London), 1937, pp. 222–235.
[47] J.C. Jaeger, Moving sources of heat and the temperature at sliding contacts, Proc. R. Soc. NSW 76 (1942) 203–224.
[48] F.D. Ju, J.H. Huang, Heat checking in the contact zone of a bearing seal (A two-dimensional model of a single moving asperity), Wear 79 (1982) 107–118.
[49] J.H. Huang, F.D. Ju, Thermomechanical cracking due to moving frictional loads, Wear 102 (1985) 81–104.
[50] N. Ye, K. Komvopoulos, Three-dimensional finite element analysis of elastic–plastic layered media under thermomechanical surface loading, J. Tribol. 125 (2003) 52–59.
[51] Z.-Q. Gong, K. Komvopoulos, Mechanical and thermomechanical elastic–plastic contact analysis of layered media with patterned surfaces, J. Tribol. 126 (2004) 9–17.
[52] H. Uetz, J. Föhl, Wear as an energy transformation process, Wear 49 (1978) 253–264.
[53] K.L. Johnson, Contact Mechanics, Cambridge University Press, Cambridge, UK, 1985.
[54] J.R. Barber, Thermoelastic displacements and stresses due to a heat source moving over the surface of a half plane, J. Appl. Mech. 51 (1984) 636–640.